

# Tunable Charge Transport in Hybrid Superlattices of Indium Tin Oxide Nanocrystals and Metal Phthalocyanines—Toward Sensing Applications

Mahdi Samadi Khoshkhoo, Yvonne Joseph, Santanu Maiti, Frank Schreiber, Thomas Chassé, and Marcus Scheele\*

Macroscopic superlattices of tin-doped indium oxide (ITO) nanocrystals (NCs) are prepared by self-assembly at the air/liquid interface followed by simultaneous ligand exchange with the organic semiconductors M-4,4',4'',4'''-tetraaminophthalocyanine (M4APc, M = Cu, Co, Fe, Ni, Zn). Transport measurements, focusing on the effect of the metal center of the ligand, reveal a ligand-dependent increase in electrical conductance by six to nine orders of magnitude, suggesting that M4APc provides efficient electronic coupling for neighboring ITO NCs. The resulting *I*–*V* characteristics as well as the temperature dependence (7–300 K) of the zero-voltage conductance indicates that at low temperatures, transport across the arrays occurs via a sequence of inelastic cotunneling events, each involving  $\approx 3$  ITO NCs. At higher temperatures, a crossover to 3D Mott-variable range hopping mechanism is observed. Finally, the vapor sensitivity of chemiresistors is investigated made from ITO NCs coupled via Cu- and Zn4APc by dosing the sensors with 4-methyl-2-pentanone (4M2P), toluene, 1-propanol, and water in the concentration range of 100–5000 ppm at 0% relative humidity. The nanocrystal superlattices respond with an increase in resistance to these analytes with the highest sensitivity to 4M2P.

## 1. Introduction

Due to their shape/size-tunable electronic and optical properties, ease of fabrication, and solution processability, colloidal semiconductor nanocrystals (NCs) have gained substantial attention as promising building blocks for advanced materials and devices. They already play a relevant role in field-effect transistors (FETs), light-emitting diodes (LEDs), photodiodes and photovoltaic cells (PVCs) as well as in biological applications, and important perspectives in future nanoelectronic and nano-optoelectronic devices are expected.<sup>[1–7]</sup> Among different classes of structures, arrays of few monolayers of NCs connected via organic ligands have recently attracted significant attention due to their numerous novel emerging applications.<sup>[3,8–10]</sup> The architecture of these devices includes inorganic nanocrystals physically and electronically connected to each other through organic semiconductor

bridges. These nanostructures have demonstrated variable sensitivity and selectivity utilizing different linker molecules which make them promising for developing artificial noses and multivariable sensors.<sup>[11–14]</sup> To this end, a fundamental understanding of charge transport in NCs arrays containing hybrid molecule–nanoparticle junctions is of particular relevance.

Charge transport in NC assemblies is often reported to follow the variable range hopping (VRH) model,  $g(T) \propto \exp[-(T_0/T)^\gamma]$ ,<sup>[15–17]</sup> where  $T_0$  is a characteristic temperature and  $\gamma = 1/2$ ,  $1/3$ , and  $1/4$  for Efros–Shklovskii (ES) or Coulomb Gap (CG), 2D, and 3D transport models, respectively. The similarity of charge transport properties in arrays of NCs versus VRH in doped semiconductors was first noticed by Beverly et al.<sup>[18]</sup> Since that observation, many experiments on metallic and semiconducting nanocrystal arrays at low temperatures (inside the Coulomb blockade regime) revealed  $\gamma = 1/2$ , suggesting that transport in these systems can be satisfactorily described by the ES-VRH model.<sup>[19–21]</sup> This model is based on direct, single-charge tunnel events between distributed defect sites. However, when applied to NC arrays, the derived hopping lengths are often equivalent to several NC diameters, which questions its applicability to arrays of NCs. Thus, an alternative picture

M. Samadi Khoshkhoo, Prof. T. Chassé, Dr. M. Scheele  
Institute of Physical and Theoretical Chemistry  
University of Tübingen

Auf der Morgenstelle 18, 72076 Tübingen, Germany

Prof. Y. Joseph

Institute of Electronic and Sensor Materials

TU Bergakademie Freiberg

Gustav-Zeuner-Straße 3, 09599 Freiberg, Germany

Dr. S. Maiti, Prof. F. Schreiber

Institute of Applied Physics

University of Tübingen

Auf der Morgenstelle 10, 72076 Tübingen, Germany

Prof. F. Schreiber, Prof. T. Chassé, Dr. M. Scheele

Center for Light-Matter Interaction

Sensors and Analytics LISA+

University of Tübingen

Auf der Morgenstelle 15, 72076 Tübingen, Germany

E-mail: marcus.scheele@uni-tuebingen.de

 The ORCID identification number(s) for the author(s) of this article can be found under <https://doi.org/10.1002/admi.201701623>.

DOI: 10.1002/admi.201701623

with the same temperature dependence has been proposed by Beloborodov et al. to explain an identical  $\frac{1}{2}$  exponent based on cooperative multielectron processes, known as the multiple inelastic cotunneling (IC) model.<sup>[22–24]</sup> In this process, the electron tunnels from an initial to a final state via virtual intermediate states.<sup>[25,26]</sup> Inelastic cotunneling can be visualized as a superposition of electron tunneling events into a nanocrystal and simultaneous escape of another electron from the same nanocrystal, creating electron–hole pairs.<sup>[27]</sup> Although these synchronized cooperative multielectron hops occur over distances of several nanoparticles, they entail only the Coulomb energy cost of roughly a single-quantum event.<sup>[28]</sup> On the other hand, the probability for such synchronized hops to occur is quite low, which negatively impacts the hopping rate. Thus, the resulting cotunneling distance is the outcome of an optimization process between the number of electron cooperative cotunneling events and the net energy cost.

The characteristics of the IC regime are affected by the properties and arrangement of the NC arrays, e.g., the diameter of nanocrystals,  $D$ , the length of the tunnel barrier or edge-to-edge interparticle distance,  $s$ , the size distribution of NCs, and the dielectric constant of the NCs environment,  $\epsilon$  (organic ligand molecules). As two examples, Kang et al.<sup>[17]</sup> have reported the influence of particle size,  $D$ , on charge transport in PbSe nanocrystal thin films while keeping  $s$  constant. Dugay et al.<sup>[29]</sup> and Moreira et al.<sup>[30]</sup> have investigated the effect of the length of the ligand molecule,  $s$ , on the characteristics of the IC regime in metallic cobalt nanoparticles and Au NCs thin films, respectively. These results indicate that investigating the sole effect of the ligand's dielectric constant on charge transport requires a set of samples with precisely the same nanocrystals and the same molecular lengths of the molecules. In this work, we present such a study by fabricating arrays of indium tin oxide (ITO) NCs crosslinked with different M4APc ( $M = \text{Cu, Co, Fe, Ni, and Zn}$ ) molecules to understand the electron transport mechanism as well as the effect of the ligands' dielectric constant, which is strongly affected by the metal center of molecule. Our results indicate that the dielectric constant of the semiconductor ligands significantly regulates charge transport, the Coulomb charging energy, and the localization length in particular. Finally, we investigate the potential of this material for vapor sensing applications. To this end, the sensor response characteristics of ITO NCs coupled via Cu- and Zn4APc are measured by dosing the films with dilute vapors of 4-methyl-2-pentanone (4M2P), toluene, 1-propanol, and water. We suggest that a combination of swelling of the NCs network and permittivity changes dominates the sensing mechanism in the superlattices.

## 2. Results

The scanning transmission electron microscopy (STEM) images of the ITO NCs thin-films before and after ligand exchange are presented in **Figure 1**. Figure 1A shows STEM images of a two monolayer thick film of myristic acid (MA)-capped ITO NCs. Figure 1B,F shows STEM images of the same film after ligand exchange with Cu-, Co-, Fe-, Ni-, and Zn4APc, respectively. STEM reveals that the NCs are self-assembled

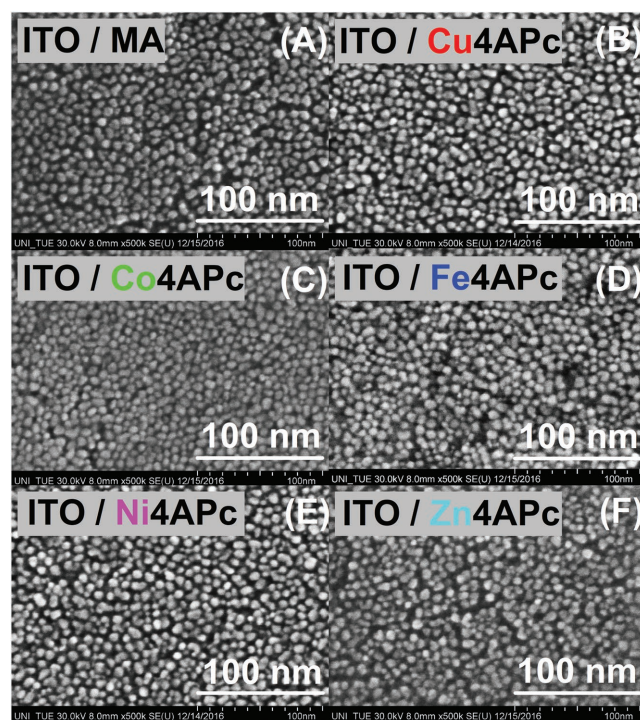


**Figure 1.** Electron microscopy images of the ITO NCs thin-films A) before and B–F) after ligand exchange with Cu-, Co-, Fe-, Ni-, and Zn4APc, respectively.

into large-areas and they are well separated from each other by either the myristic acid chains or the M4APc molecules. The results suggest that the films are not subjected to significant cracks after ligand exchange (see the lower magnification STEM images which are shown in Figures S1–S6, Supporting Information). The average particle size is found to be 6.8 nm by evaluating several STEM pictures from the same substrate and counting more than 500 particles. The histogram for size analysis can be found in Figure S7 in the Supporting Information. By using X-ray photoelectron spectroscopy (XPS), grazing-incidence small-angle X-ray scattering (GISAXS), and UV–vis–near infrared (NIR) spectroscopy, we have demonstrated that the semiconductor molecules largely replace the native surfactant from the ITO NC surface and act as crosslinkers between neighboring particles (detailed results can be found in the Supporting Information).

An estimate of the carrier concentration ( $N$ ) in the ITO NCs used in this work is obtained through the following equation<sup>[31–35]</sup>

$$\omega_p = \sqrt{\frac{Ne^2}{m_e \epsilon_0}} \quad (1)$$

where  $\omega_p$  is the plasma frequency,  $e$  is the elementary charge,  $m_e$  is the effective mass, and  $\epsilon_0$  is the vacuum permittivity. Applied to the spectroscopic data displayed in Figure S9 in the Supporting Information, we estimate the charge carrier concentration as  $9 \times 10^{18} \text{ cm}^{-3}$ , which is well placed in the range ( $10^{18}$ – $10^{22} \text{ cm}^{-3}$ ) often reported for n-type conductive metal oxides.<sup>[34–37]</sup>

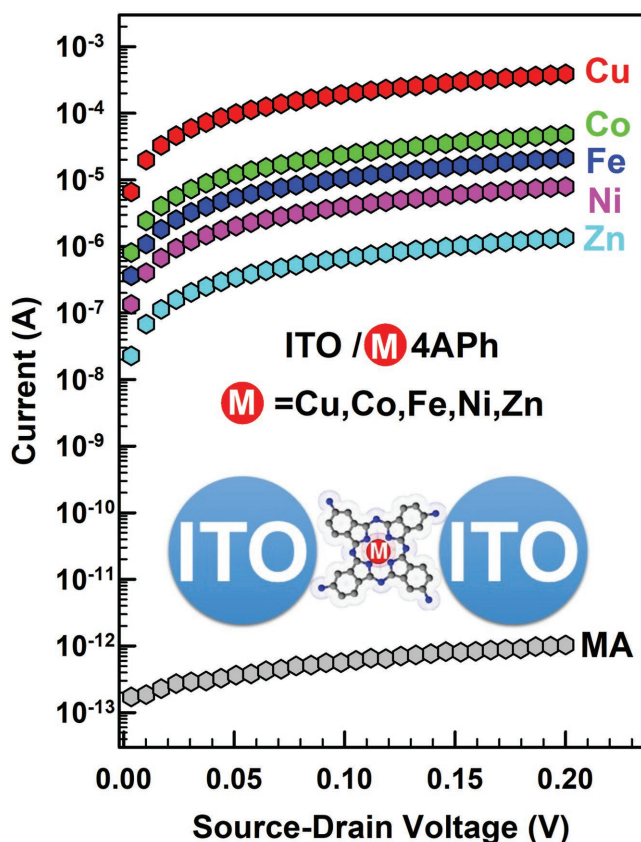


**Figure 2.** The  $I$ - $V$  characteristics measured at room temperature for ITO NCs arrays before (gray circles) and after ligand exchange to Cu- (red), Co- (green), Fe- (blue), Ni- (pink), and Zn4APc (cyan).

The electrical properties of the ITO NC films before and after ligand exchange are investigated by low-field two-point current-voltage ( $I$ - $V$ ) measurements at room temperature. We used the sheet resistance ( $R_s = Rw/l$ , where  $R$  is the measured resistance of the 2D NC arrays, with  $L$  and  $w$  the length and width of the channel between two gold electrodes) in order to compare the results. **Figure 2** shows the  $I$ - $V$  characteristics measured for ITO NCs arrays before and after ligand exchange. For the MA-capped ITO NCs, we find  $R_s = 7.0 \times 10^{14} \Omega \square^{-1}$  for the annealed film. Ligand exchange followed by annealing at 250 °C for 2 h reduces the sheet resistances to  $2.0 \times 10^6$ ,  $1.6 \times 10^7$ ,  $3.7 \times 10^7$ ,  $1.0 \times 10^8$ , and  $5.9 \times 10^8 \Omega \square^{-1}$  for thin-films exchanged to Cu-, Co-, Fe-, Ni-, and Zn4APc, respectively. Therefore, ligand exchange followed by annealing leads to a ligand-dependent increase in conductivity of the films by several orders of magnitude. It is worth pointing out that the lowest sheet resistance of the sample (observed for ITO/Cu4APc thin-film) is on the order of M $\Omega$  which is larger than any expected contact resistance. Furthermore, previously we have shown using the transmission line method that the effect of contact resistance in our system is negligible, thus, a two-point measurement is appropriate in this experiment.<sup>[38,39]</sup>

The charge carrier transport mechanism in ITO NC thin-films is investigated by analyzing the temperature-dependent  $I$ - $V$  characteristics as well as the zero-voltage conductance. **Figure 3** illustrates the power law behavior of the NC films

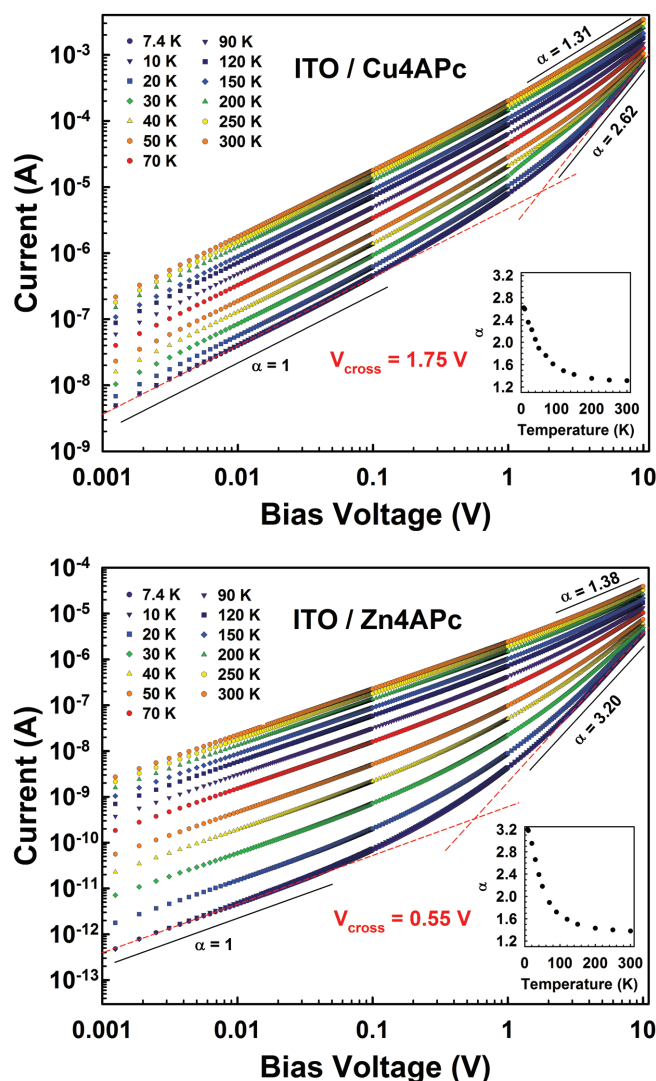


**Figure 3.** Current-voltage ( $I$ - $V$ ) characteristics as a function of temperature for ITO NCs functionalized with Cu- and Zn4APc (the solid lines are guided to the eye corresponding to the power laws with exponents as indicated). The inset graph shows the temperature-dependent change of the power law exponent.

crosslinked with Cu- and Zn4APc. The results for the films connected via ligand molecules with Co, Fe, and Ni metal centers as well as primary myristic acid ligand can be found in Figures S12 and S13 in the Supporting Information. For all samples, the conductance experiences a strong decrease of two to four orders of magnitude upon decreasing the temperature, which is typical for Coulomb blockade-dominated transport in NCs arrays. All samples exhibit a characteristic crossover voltage, indicating the transition point from ohmic ( $I \propto V$ ) to power-law ( $I \propto V^\alpha$ ,  $\alpha$  = power-law exponent) behavior. At small bias voltages, the  $I$ - $V$  characteristics obey ohmic behavior in the whole temperature range for all samples, while at large bias, the  $I$ - $V$  characteristics follow power-law behavior with a temperature-dependent exponent. **Figure 3** also reveals that the strongly temperature-dependent behavior at small bias voltages transposes into a much less temperature-dependent one

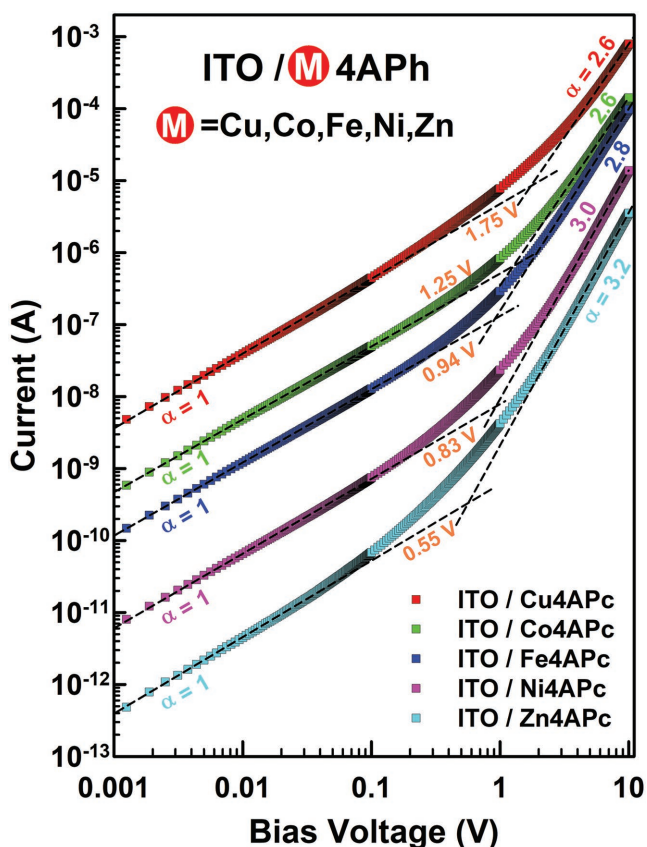


**Figure 4.** The transition from the ohmic to the nonlinear power law behavior of the NC films crosslinked with Cu-, Co-, Fe-, Ni-, and Zn4APc at 10 K.

at higher biases for all samples. In this regime, the electron transport become more field driven.<sup>[21,40]</sup> **Figure 4** illustrates the transition from the ohmic to the nonlinear power law behavior of the NC films crosslinked with Cu-, Co-, Fe-, Ni-, and Zn4APc at 10 K. As the samples become more insulating, the power law exponent at large bias voltages increases. Simultaneously, the crossover voltage decreases to lower voltages.

**Figure 5** shows the zero-voltage conductance,  $g(T)$ , plotted versus  $T^{-1/4}$  and  $T^{-1/2}$  for ITO NCs thin films after ligand exchange. We obtained  $g(T)$  of each superlattice at specific temperatures by linear fitting of the  $I$ - $V$  characteristics at small bias ( $-50$  to  $50$  mV). The result for the film before ligand exchange is reported in **Figure S15** in the Supporting Information. As expected, all the samples show semiconducting behavior in the whole measured temperature range. Evidently, the dependence of  $g(T)$  with temperature changes drastically upon exchange with different ligands. At the same time,  $g(T)$  increases monotonically with temperature.

As a consistency check, we also provide a plot of the logarithmic derivative  $w = d(\log G_{V=0})/d(\log T)$  against temperature on a

double logarithmic scale (**Figure S16**, Supporting Information) to verify our choice of exponents for the different temperature regimes.<sup>[19,41]</sup> At low temperatures, the zero-voltage conductance for all samples follows  $g(T) = g_0 \exp[-(T_0/T)^{1/2}]$  which has the same functional form as ES-VRH behavior (**Figure 5B**). The region for which we observe this functional form is gradually shifted to lower temperatures for more insulating samples. At high temperatures, the zero-voltage conductance for all samples except ITO/Cu4APc follows  $g(T) = g_0 \exp[-(T_0/T)^{1/4}]$  which has the same functional form as 3D Mott-type behavior (**Figure 5A**). The array of ITO NCs functionalized with Cu4APc shows the same functional form as the ES-VRH behavior in the whole temperature range (**Figure S16B**, Supporting Information). Fits indicated by the dashed lines give the characteristic temperature,  $T_0$ , which is summarized in **Table 1**. For more insulating samples, higher values for characteristic temperatures are obtained. Furthermore, as the samples become more insulating, deviations from Mott-type behavior, i.e., the crossover temperature ( $T_{\text{cross}}$ ) from Mott-type to ES-type behavior, occurs at increasingly lower temperatures (see **Table 1**). The prefactor,  $g_0$ , includes the tunneling through the barrier created by the ligand molecule layer capping ITO NCs. It can be considered as the attempt frequency of electrons trying to escape the nanoparticles. This prefactor decreases with the order  $\text{Cu} > \text{Co} > \text{Fe} > \text{Ni} > \text{Zn}$ .

As mentioned before, charge transport properties in NC arrays can be significantly affected by the interparticle distance of the nanocrystals (width of the tunnel barrier) as well as the dielectric constant of the environment (height of the tunnel barrier). Therefore, changing one or both of these parameters by an external stimulus (e.g., vapor sorption) can vary the transport properties of the system (e.g., overall resistance of the superlattice). **Figure 6A,B** shows the typical response of the films upon three exposures of 120 s to 4M2P for ITO/Cu4APc and ITO/Zn4APc as the most conductive and the most insulating superlattice, respectively. The sensor responses are expressed as the relative differential resistance response; that is, the change in the resistance,  $\Delta R$ , divided by the baseline resistance,  $R_0$ . In all

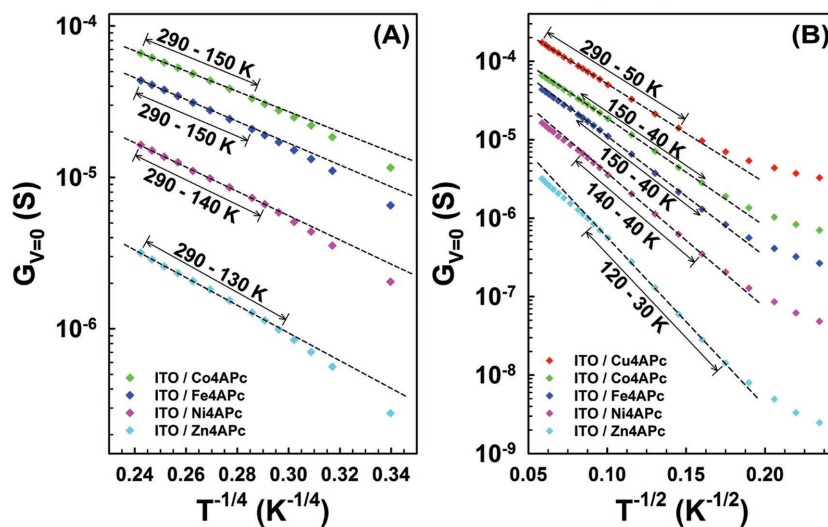


**Figure 5.** Temperature-dependent zero-voltage conductance of ITO NCs functionalized with Cu-, Co-, Fe-, Ni-, and Zn4APc plotted versus A)  $T^{-1/4}$  and B)  $T^{-1/2}$  (fits indicated by the dashed lines).

**Table 1.** The characteristic temperatures ( $T_0$ ), the exponential prefactors ( $g_0$ ), the Coulomb gap ( $\Delta_{CC}$ ), the crossover temperature ( $T_{cross}$ ), the ratio of mean hopping distance ( $R_{hop,Mott}$ ) to localization length ( $\xi$ ), and the mean hopping energy difference between sites ( $E_{hop,Mott}$ ) for MA-capped ITO NC superlattices before and after ligand exchange to Cu-, Co-, Fe-, Ni-, and Zn4APc.

Sample	$g \propto T^{-1/4}$ behavior			$T_{cross}$ [K]	$g \propto T^{-1/2}$ behavior
	$T_0$ [K]/ $g_0$ [S]	$R_{hop}/\xi$	$E_{hop}$ [meV]		
ITO/Cu4APc	–	–	–	–	$841/9.33 \times 10^{-4}$
ITO/Co4APc	$56\,228/2.76 \times 10^{-3}$	1.40	23.3	$\approx 150$	$1004/4.46 \times 10^{-4}$
ITO/Fe4APc	$75\,498/2.43 \times 10^{-3}$	1.50	25.1	$\approx 150$	$1243/3.76 \times 10^{-4}$
ITO/Ni4APc	$115\,730/1.42 \times 10^{-3}$	1.68	27.9	$\approx 140$	$1566/1.96 \times 10^{-4}$
ITO/Zn4APc	$191\,823/5.04 \times 10^{-4}$	1.90	31.7	$\approx 125$	$2433/7.86 \times 10^{-5}$
ITO/MA	$648\,434/3.58 \times 10^{-6}$	2.58	42.9	$\approx 150$	$5385/4.41 \times 10^{-7}$

cases, a fast (few seconds) and fully reversible, approximately rectangular response is observed. In order to investigate the chemical selectivity of the NC superlattices, the samples were also exposed to toluene, 1-propanol, and water vapor analytes. Figure 6C represents the response of the samples to 3200 ppm of four analytes. For all analytes, ITO/Zn4APc shows less sensitivity in comparison to ITO/Cu4APc. A decreasing sensitivity from  $Cu^{2+}$  to  $Zn^{2+}$  has also been observed and reported for the liquid sensing properties of a set of phthalocyanines (Pcs).<sup>[42]</sup> Furthermore, in both cases the sensitivities to toluene, 1-propanol, and water vapors are quite similar and lower than the response of the samples to 4M2P vapor.

### 3. Discussion

#### 3.1. Characterization of the Arrays of ITO NCs before and after Ligand Exchange

We have shown how the incorporation of Cu4APc into an array of ITO NCs can be achieved by a Langmuir-type assembly at the liquid/air interface in our previous work.<sup>[43]</sup> Here, the same property is used to introduce tetraaminophthalocyanines containing different metal centers into the arrays of ITO NCs allowing to study the effect of the metal center on the conductance increase of the films. Initially, the nanoparticles are capped by MA. During the ligand exchange process, the incoming M4APc molecules penetrate the floating NC superlattice films, replace the MA molecules, and bind to the NCs. The obtained XPS and UV–vis–NIR results clearly demonstrate that the new incoming ligand molecules are present in the structure of thin-films after ligand exchange (Figures S8 and S9, Supporting Information). In agreement with XPS and UV–vis–NIR, our GISAXS results also confirm the successful ligand exchange. The average correlation distance between neighboring NCs (center to center distance) is reduced by  $\approx 0.7 \pm 0.1$  nm (see Figures S10 and S11 as well as Table S2, Supporting Information) upon ligand exchange, matching the difference between the molecular lengths of MA and the new M4APc molecules. As demonstrated by STEM images as well as GISAXS results, ligand exchange does not disturb the structural order of the NC arrays. For all samples after ligand exchange and annealing, we observe a total redshift of 18–62 meV of the localized surface plasmon resonance, depending on the metal center of the ligand (see Table S1,

Supporting Information). We attribute this bathochromic shift to: (i) decreasing the distance between ITO NCs due to a growing interaction of the surface electrons and (ii) changes in the dielectric environment of the surface electrons. All these evidences as well as the strong increase in conductance demonstrate that M4APc acts not only as a spacer but also as an electronic linker, which greatly facilitates transport between adjacent nanocrystals.

#### 3.2. Correlation between Dielectric Environment and Transport Properties

The ligand-dependent increase in conductivity of M4APc-capped ITO NC thin films can be understood in terms of a reduction of the tunneling barrier height. At room temperature, transport occurs via sequential tunneling which is dominated by independent electron hops from one ITO nanocrystal to its nearest neighbor along the current path (Figure 7A). In sequential tunneling, the electron–hole pair is separated by one particle. The Coulomb charging energy of a nanoparticle,  $E_C$ , which is defined as the energy needed to add an excess electron onto an electronically neutral nanoparticle, is approximated by<sup>[44]</sup>

$$E_C = \frac{e^2}{4\pi\epsilon\epsilon_0 a} \quad (2)$$

where  $\epsilon$  is the dielectric constant and  $a$  is the particle radius. Different methods and models<sup>[45–50]</sup> are reported in order to estimate the Coulomb charging energy in the array of nanoparticles but in general it can be affected by (i) the particle core size, (ii) the interparticle distance, (iii) the number of nearest neighbors, and (iv) the dielectric constant of the ligand molecules.<sup>[45]</sup> Based on our STEM images and GISAXS results, the structural and geometrical properties of ITO/M4APc thin-films are very similar, and thus, the first three parameters should be almost identical for all the samples. Therefore, the sheet resistance in ITO NC networks is expected to be correlated to the dielectric environment,  $\epsilon$ . To the best of our knowledge, no values of dielectric constants are reported yet for M4APcs; however, one can find the respective data for metal-phthalocyanines, which can be used as a rough estimation for a qualitative discussion. In this respect, the dielectric constant values of 1.58, 1.7–2.7, 3.1, and 3.6 are reported for Zn-, Ni-, Co-, and Cu-phthalocyanine at room temperature, respectively.<sup>[51–55]</sup> According to Equation (2),

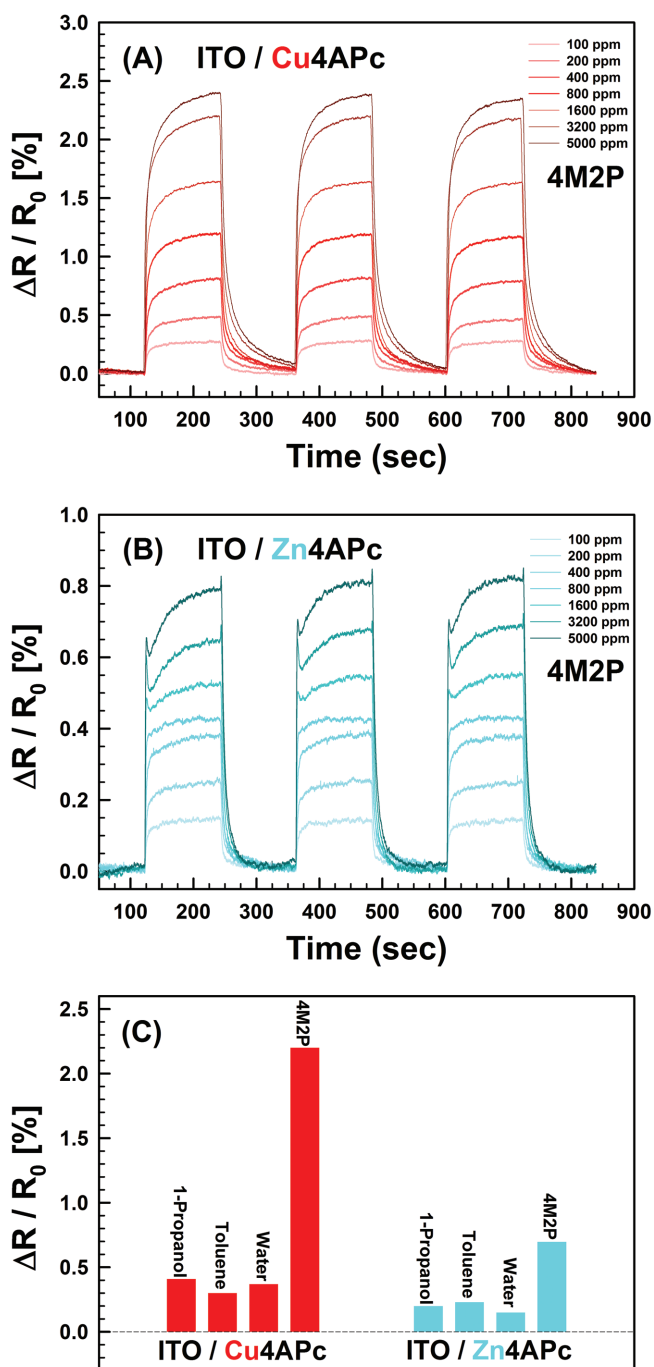


**Figure 6.** A,B) Response traces of ITO/Cu4APc and ITO/Zn4APc films toward 100–5000 ppm of 4M2P at 0% relative humidity. C) Responses traces of ITO/Cu4APc and ITO/Zn4APc films toward 3200 ppm of 4M2P, toluene, 1-propanol, and water vapors.

smaller  $\epsilon$  implies larger  $E_C$  and thus a significant suppression of tunneling in arrays of NCs. For NC arrays connected via Cu4APc, due to the higher dielectric constant of the environment, the Coulomb interaction is screened and electrons can propagate more easily. This explanation supports the order of conductance values observed for the array of ITO NCs coupled via M4APc (Cu > Co > Fe > Ni > Zn) and demonstrates that a

decrease in resistance is caused by an increase in the average permittivity of the nanocrystals' environment.

### 3.3. Charge Transport at High Temperatures

In order to fully characterize the mechanisms of transport, we varied the temperature (7–300 K) and the bias voltage (0.001–10 V) over a wide range. The conductance data of the arrays at high temperatures were primarily analyzed using the thermal activation model  $g(T) \approx \exp[-E_a/k_B T]$ , where  $E_a$  is the activation energy and  $k_B$  is the Boltzmann constant. However, the fitting quality was poor indicating that this model is not applicable here. Instead, the transport data fit well to the 3D Mott-VRH mechanism ( $g(T) = g_0 \exp[-(T_0/T)^{1/4}]$ ) except for ITO/Cu4APc, which follows  $g(T) = g_0 \exp[-(T_0/T)^{1/2}]$  within the whole temperature range. For the Mott-VRH theory to be valid, the mean hopping distance,  $R_{\text{hop,Mott}}$ , must be larger than the localization length,  $\xi$ , thus the ratio  $R_{\text{hop,Mott}}/\xi = 3/8[T_{\text{Mott}}/T]^{1/4}$  should be larger than unity.  $\xi$  characterizes the tunneling probability between nearest sites and longer values represent smaller barrier height between the nanocrystals. In all cases, the calculated  $R_{\text{hop,Mott}}/\xi$  values (see Table 1) are larger than 1, thus satisfying the criterion of the Mott-VRH model. Knowledge of the Mott characteristic temperature also provides the mean hopping energy difference between sites,  $E_{\text{hop,Mott}} = 1/4 k_B T [T_{\text{Mott}}/T]^{1/4}$ , which are on the order of few tens of meV (see Table 1). Depending on the ligand metal center, the mean hopping energy difference between sites increases from Co- to Zn4APc capped ITO NCs (Zn > Ni > Fe > Co).

Based on the variable range hopping model prediction, VRH should evolve from the Mott-type regime,  $T^{-1/4}$ , at higher temperatures to ES-type behavior,  $T^{-1/2}$ , at thermal energies smaller than the width of the Coulomb gap.<sup>[56]</sup> The clear crossover from Mott- to ES-VRH-type behavior observed in our samples indicates the opening of a soft Coulomb gap at low temperatures,  $\Delta_{\text{CG}}$ .<sup>[16]</sup> This crossover has been also observed for bulk indium oxide films<sup>[57]</sup> as well as CdSe quantum dots films.<sup>[19]</sup> The transition temperature between these charge transport mechanisms is observed to depend on the metal center of the connecting ligand in this work with the transition taking place at higher temperatures for more conductive samples.

### 3.4. Charge Transport at Low Temperatures

With decreasing the temperature, the  $I$ - $V$  characteristics become more nonlinear (see Figure S14, Supporting Information). The more pronounced nonlinear behavior for more insulating samples at low temperatures can be attributed to the lower dielectric constant of the NCs environment, and thus, higher charging energy between them. Furthermore, consistent with other measurements on nanoparticle arrays, the current starts to be suppressed in the low bias region, which is considered to be the consequence of the Coulomb blockade. When the Coulomb blockade regime dominates, cooperative tunneling of several charges through  $N_{\text{cot}}$  junctions becomes significant (Figure 7B), and this is known as the multiple inelastic cotunneling mechanism. The current

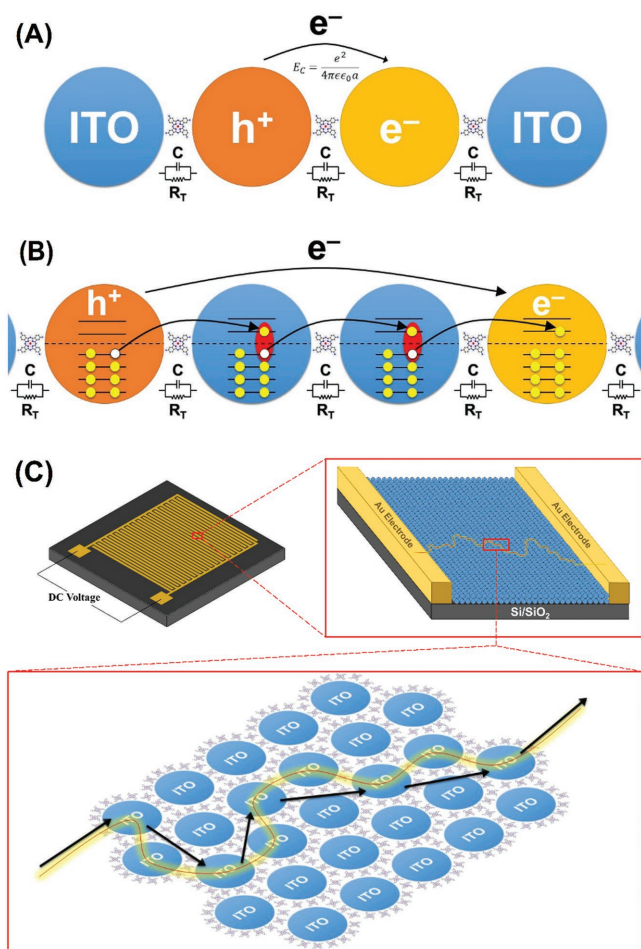


**Figure 7.** Schematic representation of A) sequential tunneling, B) inelastic cotunneling, and C) electron transport in nanocrystal array via inelastic cotunneling (black arrows) along paths that optimize the overall energy costs.

flow in this type of charge transport is given by a Taylor series proposed by Tran et al.<sup>[24]</sup>

$$I \propto V_{\text{jct}} \sum_j \left( \frac{\hbar}{e^2 R_T} \right)^j \left( \frac{k_B^2 T^2 + e^2 V_{\text{jct}}^2}{E_C^2} \right)^{j-1} \exp \left( - \frac{E_C - j e V_{\text{jct}}}{k_B T} \right) \quad (3)$$

Here,  $T$  is the temperature,  $k_B$  is Boltzman constant,  $R_T$  is the resistance of a single junction, and  $V_{\text{jct}}$  is the voltage drop over a single tunneling junction connecting two neighboring nanocrystals. Based on Equation (3), Dayen et al.<sup>[40]</sup> have found that when the thermal energy becomes smaller than the Coulomb charging energy, the electronic behavior during cotunneling can be split into three regimes depending on different voltage ranges between neighboring nanocrystals

$$C1: I \propto V \quad e V_{\text{jct}} < k_B T \quad (4a)$$

$$C2: I \propto V^\infty \quad k_B T < e V_{\text{jct}} < k_B T \ln \left( \frac{e^2}{\hbar} R_T \right) \quad (4b)$$

$$C3: I \propto \exp \left( \sqrt{\frac{V^*}{V}} \right) k_B T \ln \left( \frac{e^2}{\hbar} R_T \right) < e V_{\text{jct}} \quad (4c)$$

where  $V^*$  is a characteristic voltage. The number of junctions across the gap between the electrodes in our system is  $\approx 300$ , thus, the global Coulomb blockade threshold  $V_t \approx N E_C$  can easily reach several volts. In an ideal case by considering the straight path between the electrodes, the applied bias voltage and the bias per junction are related by  $V_{\text{jct}} = V/n$ , where  $n$  is the number of junctions involved in transport. Therefore, based on Equation (4a) and by considering the number of NCs present across the gap between the electrodes ( $\approx 300$ ), at  $T = 10$  K we expect a linear behavior at a bias voltage less than  $\approx 0.25$  V. This is indeed what we find in Figure 4.

At higher bias voltages (i.e.,  $k_B T < e V_{\text{jct}} < k_B T \ln[e^2 \hbar / R_T]$ ), the data are fitted well by power laws of the form  $I \propto V^\alpha$ , in line with Equation (4b). At 10 K, the exponents are  $\approx 3.2, 3, 2.8, 2.6$ , and  $2.6$  for ITO NCs array crosslinked by Zn-, Ni-, Fe-, Co-, and Cu4APc, respectively. The greatest power-law exponent of  $\approx 4.3$  is obtained for MA-capped ITO NCs thin-films at 10 K (see the Supporting Information). The cotunneling distance, which is a characteristic length scale, invokes the curvature of the nonlinear  $I$ - $V$  characteristics as well as the temperature dependence of the zero-voltage conductance. The number of cotunneling events,  $N_{\text{cot}}$ , relates as  $\alpha = 2N_{\text{cot}} - 1$ ; therefore, the typical number of the junctions participating in the cotunnel events are 2.1, 2, 1.9, 1.8, and 1.8 for the NC films connected via ligand molecules with Zn, Ni, Fe, Co, and Cu metal centers, respectively. For MA-capped ITO NCs thin-films, the number of junctions involved is 2.65. This indicates that at low temperatures, transport across the arrays occurs via a sequence of cotunneling events, each involving  $\approx 3$ –4 ITO NCs (schematically shown in Figure 7C). The necessity for multiple cotunneling events arises from the fact that the number of NCs participating in one cotunneling event ( $\approx 3$ –4) is much lower than the number of NCs present across the gap between the electrodes ( $\approx 300$ ). Inelastic cotunneling takes over inside the Coulomb blockade regime, while at high temperatures and/or at large bias voltage above the global Coulomb blockade threshold,  $e V_{\text{jct}} \approx E_C$ , transport occurs via sequential tunneling. The range of cotunneling hops changes with temperature. As apparent in Figure 3, at higher temperatures the power-law exponent decreases toward unity, which means that the number of hops decreases to one and cotunneling behavior makes way for sequential tunneling.

For further investigation of the transport mechanism in the superlattices, the temperature dependence of the zero-voltage conductance (Figure 5) was studied. The positive temperature coefficient of the zero-voltage conductance is a significant feature of an insulator. For low temperatures above 30 K, a good linear relationship is found in the  $\ln[g(T)]$  versus  $(1/T)^{1/2}$  plot which arises from multiple inelastic cotunneling.<sup>[29]</sup> We note that for  $T < 30$  K in Figure 5B, the change in slope indicates a slightly altered transport mechanism, which we tentatively attribute to the gradual onset of elastic cotunneling.<sup>[22]</sup>

Within the framework of inelastic cotunneling, the temperature dependence of the conductance follows<sup>[23,24]</sup>

$$g = g_0 \exp \left[ - (T_0 / T)^{1/2} \right] \quad (5)$$

where  $T_0$  is the activation temperature and is linked to the Coulomb charging energy,  $E_C$ , through  $T_0 = CE_c/(k_B\xi)$ . Here,  $\xi$  is the localization length and  $C$  is a numerical constant ( $C \approx 2.8$  for 3D). From the conductance versus temperature behavior, several characteristic parameters describing charge transport in the array of ITO NCs can be extracted. For our experimental data, the fits of the conductance yield  $T_0 = 841, 1004, 1243, 1566,$  and  $2433$  K for ITO NCs array coupled via Cu-, Co-, Fe-, Ni-, and Zn4APc, respectively. Obviously, the increase in the activation temperature is related to the role of the metal center of the connecting ligand molecule, as the geometrical properties of the ITO/M4APc thin-films are very similar in all the samples. The localization length in the inelastic cotunneling regime can be calculated as<sup>[17,23,24]</sup>

$$\xi = \frac{Ce^2}{4\pi\epsilon\epsilon_0k_B T_0} \quad (6)$$

using the measured activation temperature,  $T_0$ , and the estimated dielectric constant of the environment. However, it can be also calculated independent of the dielectric constant via the number of cotunneling events,  $N_{cot}$  (from the curvature of  $I$ - $V$  characteristics) as well as the activation temperature,  $T_0$ , through equating  $N_{cot}$  to the number of junctions involved in a typical hop<sup>[23,24,29,58,59]</sup>

$$N_{cot} = \frac{r^*}{d} = \left( \frac{e^2\xi}{4\pi\epsilon\epsilon_0k_B T} \right)^{1/2} \frac{1}{d} = \left( \frac{T_0}{CT} \right)^{1/2} \frac{\xi}{d} \quad (7)$$

Here,  $d$  is the average interparticle distance (estimated as 8.0 nm by GISAXS). At  $T = 50$  K, we find  $2.36 \text{ nm} < \xi < 4.70 \text{ nm}$  depending on the connecting ligand between ITO NCs (see Table 2), which is in the range of observed values for closed-pack arrays of metallic or semiconductor nanoparticles.<sup>[21,23]</sup> The localization length calculated for ITO/M4APc thin-films characterizes the overlap of the wave functions between different sites. It is essentially defined as the decay length of an electron in NCs assemblies. In all cases, it is larger than the nanocrystal separation (i.e., edge-to-edge interparticle distance of  $\approx 1.2$  nm). The greatest obtained localization length for ITO/Cu4APc reflects the strongest correlation of the electronic wave function in that case. Having the localization length, one can calculate the dielectric constant of the environment using the localization length and the activation temperature from Equation (6).<sup>[16]</sup> At 50 K, the calculated dielectric constant values decrease from

**Table 2.** The number of cotunneling events ( $N_{cot}$ ), electron localization length ( $\xi$ ), dielectric constant of the environment ( $\epsilon$ ), and the Coulomb charging energy ( $E_c$ ) for arrays of MA-capped ITO NCs before and after ligand exchange to Cu-, Co-, Fe-, Ni-, and Zn4APc at 50 K.

Sample	$N_{cot}$	$\xi$ [nm]	$\epsilon$	$E_c$ [meV]/K
ITO/Cu4APc	1.44	4.70	11.83	35.8/≈415
ITO/Co4APc	1.46	4.36	10.68	39.6/≈460
ITO/Fe4APc	1.49	4.00	9.40	45.0/≈522
ITO/Ni4APc	1.53	3.65	8.16	51.9/≈602
ITO/Zn4APc	1.59	3.05	6.30	67.2/≈780
ITO/MA	1.83	2.36	3.68	115.0/≈1335

11.83 for ITO NCs connected via Cu4APc to 6.30 for the arrays interlinked by Zn4APc (Cu > Co > Fe > Ni > Zn). The order is in good agreement with that observed in phthalocyanines (see Section 4.2 and refs. [51–55]). This shows that the metal center of the ligand can significantly affect the dielectric constant of the molecule, and thus, the Coulomb charging energy of NCs. We note that the rather large values obtained for the dielectric constants in comparison to those reported for metal Pcs might arise from three reasons: (i) in M4APcs, there are four additional polar amino groups which can significantly alter the dielectric behavior of the molecule; (ii) the model considers the simple self-capacitance of NCs in order to calculate the charging energy which can be improved by including the mutual capacitance arising from nearest-neighbor interactions to the total capacitance; and (iii) the calculations for M4APcs in this work are carried out for  $T = 50$  K; however, the results reported for metal Pcs correspond to room-temperature measurements. The temperature dependence of dielectric constants is well documented for isotropic or cubic inorganic materials<sup>[60]</sup> and was also recently reported for CuPc<sup>[61]</sup> and Pc derivatives.<sup>[62]</sup> Using the conductivity pre-exponential factor,  $g_0$ , we can describe the hopping rate between nanocrystals. This prefactor decreases for M4APc-coupled ITO NCs arrays along the order Cu > Co > Fe > Ni > Zn, demonstrating that the number of hops necessary for charge transport as well as interparticle coupling between NCs decrease in the mentioned order. Therefore, our results demonstrate that arrays of nanocrystals coupled by organic connecting ligands with larger dielectric constants exhibit weaker temperature dependence (see Figure 3) as well as higher conductivity (see Figure 2) in line with previous expectations.<sup>[21]</sup>

The occurrence of cotunneling and the ability to fine-tune the number of junctions involved in this process open new opportunities for device applications.<sup>[40,63]</sup> Conduction via inelastic cotunneling can increase the sensitivity of the sample to an external stimulus, since the resistance will be proportional to  $R_T^{N_{cot}}$  (where  $R_T$  is the resistance of a simple NC–molecule–NC junction). Well-documented examples include spin-dependent resistance in magnetic systems enhanced by cotunneling<sup>[63,64]</sup> as well as the enhanced tunnel magnetoresistance in spintronic systems.<sup>[65–67]</sup>

### 3.5. Vapor Sensing Properties

One major aim of this study was to demonstrate the potential applicability of coupled ITO/M4APc structures in sensing applications. The results shown in Figure 6 clearly demonstrate that the ITO NC superlattices connected via both Zn- and Cu4APc respond (with an increase in resistance) to all four analytes with highest sensitivity to 4M2P. The vapors we have used in this study cover different classes of analytes: hydrophilic hydrocarbons (4M2P), hydrophobic hydrocarbons (toluene), H-bonding organic compounds (1-propanol), and polar H-bonding inorganic compounds (water). Furthermore, different dielectric constant of these analytes (water: 80.1, 1-propanol: 20.8, 4M2P: 13.11, and toluene: 2.4 at 20 °C<sup>[68]</sup>), together with their different classes, render them well suited to study the chemical selectivity of the sensor samples. Considering the nanostructure of our superlattice, one can find four possible binding sites with very different

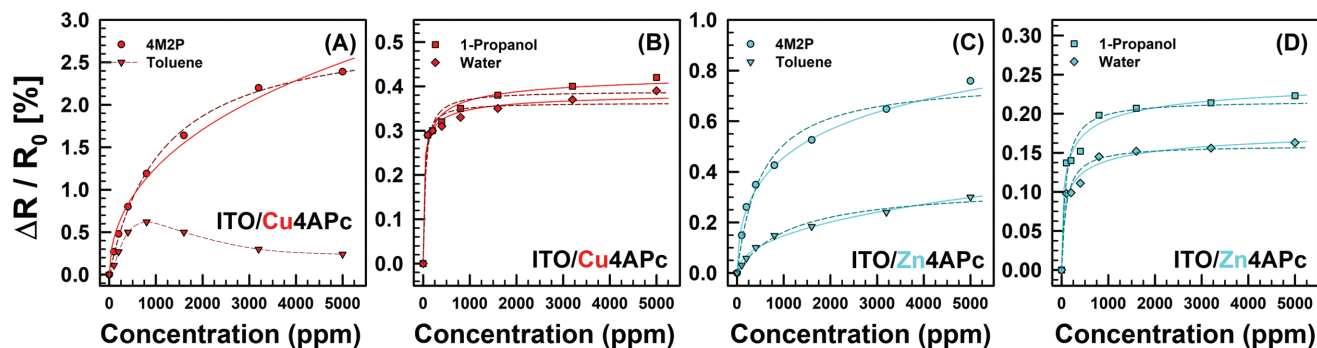


**Figure 8.** Response isotherms of A,B) ITO/Cu4APc and C,D) ITO/Zn4APc superlattices indicating concentration-dependent responses to 100–5000 ppm of analytes. The dashed lines are the Langmuir fits according to a 1st order adsorption model (i.e., Equation (8)) and the solid lines are the Langmuir fits according to a 2nd order adsorption model (i.e., Equation (9)). In the case of ITO/Cu4APc exposed to toluene, the dashed line is a guide to the eye.

chemical nature: (i) vacant sites on ITO nanocrystals that contain hydroxyl groups or oxygen bridges,<sup>[43]</sup> (ii) four amino functional groups of each linker molecule which can be unbound or bound to the surface of the nanocrystals,<sup>[43]</sup> (iii) the metal center (Cu or Zn) of the linker molecules, and (iv) the hydrophobic backbone of the ligands in between the nanocrystals. **Figure 8** indicates the response isotherms for the films of ITO/Cu4APc and ITO/Zn4APc superlattices for analyte concentrations from 100 to 5000 ppm. In agreement with the literature,<sup>[54]</sup> we fitted the data points with a Langmuir adsorption model which has been described previously by Barlett and Ling-Chung according to the following equation (see Figure 8)<sup>[69]</sup>

$$\frac{\Delta R}{R_0} = \left[ \frac{\Delta R}{R_0} \right]_s \frac{K_b C_{\text{vapor}}}{1 + K_b C_{\text{vapor}}} \quad (8)$$

where  $[\Delta R/R_0]_s$  is the relative change of resistance at saturation,  $K_b$  is the binding constant, and  $C_{\text{vapor}}$  is the concentration of the analyte in the gas phase. The data measured for the films of ITO/Cu4APc exposed to 4M2P and ITO/Zn4APc exposed to toluene fit fairly well to the Langmuir adsorption model according to Equation (8) (solid lines in Figure 8). Using the first order of Langmuir adsorption model for ITO/Cu4APc exposed to 1-propanol and water and ITO/Zn4APc exposed to 4M2P, 1-propanol, and water, we recognize some deviations in the fittings; therefore, the data were also fitted using the second order Langmuir adsorption model based on the following equation (see Figure 8)

$$\frac{\Delta R}{R_0} = \left[ \frac{\Delta R}{R_0} \right]_s \frac{K_b \sqrt{C_{\text{vapor}}}}{1 + K_b \sqrt{C_{\text{vapor}}}} \quad (9)$$

This model gives even better fits to the measured data. The relative differential resistance response at saturation  $[\Delta R/R_0]_s$  and the binding constants  $K_b$  obtained from the 1st and 2nd order Langmuir adsorption model are tabulated in **Table 3**. As seen by the  $[\Delta R/R_0]_s$ -values, the highest sensitivity is detected for superlattices exposed to 4M2P. The higher response amplitudes of both superlattices to 4M2P might be the result of larger partitioning of analyte in

the films. This is in agreement with the nature of the M4APc molecule (partly polar and hydrophobic with a minor ability to form hydrogen bonds), that is expected to be the sorption site for the vaporous analytes.<sup>[70]</sup> Although the  $[\Delta R/R_0]_s$ -value is rather low, the high signal-to-noise ratio of the response curves (Figure 6) suggests that the detection limit for this system can well go below 100 ppm. The lower sensitivity values observed for all analytes in the case of ITO/Zn4APc compared to ITO/Cu4APc can be attributed to the weaker interaction capabilities of metal center ions of ligands with analyte molecules.<sup>[42]</sup> The stronger curvature of the response isotherms for both superlattices exposed to 1-propanol and water (Figure 8B,D) indicates that these analytes bind significantly stronger to the nanostructure than 4M2P and toluene. This can also be deduced from the higher binding constants  $K_b$  obtained by fitting (e.g., for ITO/Zn4APc; see Table 3). The ligand molecules, Cu- and Zn4APc, have an aromatic nature with a high delocalization of  $\pi$ -electrons, and thus, the adsorption of toluene probably occurs by weak physisorption involving noncovalent  $\pi$ - $\pi$  stacking interactions.<sup>[71]</sup> We argue that hydrophobic 4M2P and toluene adsorb to the nanostructure by swelling in the organic matrix (by adsorption on the hydrophobic backbone of the ligands in between the nanocrystals), and thus, behave more vapor-like. In contrast, 1-propanol and water behave more gaseous-like in their interaction with the metal center of the M4APc

**Table 3.** The relative differential resistance response at saturation  $[\Delta R/R_0]_s$  and the binding constants  $K_b$  obtained from the 1st and 2nd order Langmuir adsorption model according to Equations (8) and (9), respectively. The numbers in parenthesis demonstrate the better fitting results in each case.

NC film	Analyte	1st order kinetics		2nd order kinetics	
		$[\Delta R/R_0]_s$ [%]	$K_b$ [ $\text{M}^{-1}$ ]	$[\Delta R/R_0]_s$ [%]	$K_b$ [ $\text{M}^{-0.5}$ ]
ITO/Cu4APc	4M2P	(2.92)	(88.59)	12.35	1.14
	Toluene	–	–	–	–
	1-propanol	0.39	1201.90	(0.44)	(38.34)
	Water	0.36	532.53	(0.39)	(30.29)
ITO/Zn4APc	4M2P	0.77	191.90	(1.52)	(4.30)
	Toluene	(0.35)	(81.27)	1.80	0.85
	1-propanol	0.21	680.87	(0.25)	(23.43)
	Water	0.16	187.90	(0.19)	(11.99)

linkers, reaching saturation when every metal center is occupied. In line with this argument, it has been shown that water vapor acts as an effective donor on metal phthalocyanine surfaces,<sup>[72,73]</sup> and simulations have demonstrated that only two water molecules on average may be placed in the neighborhood of the metal center.<sup>[74]</sup> One might also expect the adsorption of analytes on the possible binding sites present on the nanocrystals surface; however, since most of the surface is covered by ligand molecules, diffusion and adsorption on these sites are quite challenging for analyte molecules due to steric hindrance as well as the limited number of free available sites. It also has to be noted that all measurements were carried out on dry purified air as carrier gas at room temperature. As shown, water sorbs to the material and it can be assumed that measurements under ambient conditions at higher humidity levels will lead to a blockage of the water sorption sites and will influence the sorption of other analytes competing with water for the same sites. However, detailed investigations on this cross sensitivity and also on sensitivity changes due to temperature variations are beyond the scope of this work and should be addressed in the future.

Considering the positive response (resistance increase) of the films and the charge transport at high temperatures discussed in the previous part, we propose that swelling can be one dominating component of the sensing mechanism in the presented materials. Accordingly, swelling of the superlattice network during vapor sorption leads to an increase in the interparticle tunnel distance, which in turn results in an increased tunneling barrier height and, thus, an increased resistance.<sup>[75,76]</sup> Furthermore, one should consider that the response of the superlattices can also be determined by the change in dielectric constant of the environment of the nanocrystals. As shown in previous sections, a change in dielectric constant of the environment can significantly modulate the charge transport properties of the system. Since the mixture of swelling and permittivity changes play major roles in sensing mechanisms, distinguishing the contribution and importance of each factor needs more systematic experiments, which will be subject to a forthcoming publication. In the case of ITO/Cu4APc superlattices exposed to toluene, the Langmuir adsorption model cannot describe the behavior satisfactorily. By increasing the vapor concentration, we first observe an increase in the relative change of resistance followed by a decrease at higher vapor concentrations (see Figure 8A), suggesting the existence of a competition between at least two different parameters in this special system that requires more investigations in future works.

## 4. Conclusion

In this work, we expanded the choice of the metal center of M4APc (M = Cu, Co, Fe, Ni, and Zn), incorporated them into an array of ITO NCs by a Langmuir-type assembly at the liquid/air interface and studied the electron transport mechanism in the NC arrays. Two-point probe conductivity measurements revealed that ligand exchange leads to a ligand metal-center-dependent increase in conductance of thin-films by six to nine orders of magnitude. It was shown that the decrease in resistance (in ITO superlattices connected via M4APc with

different metal centers) is caused by an increase in the average permittivity of the nanocrystals' environment. The resulting *I*-*V* characteristics as well as the temperature-dependent conductivity measurements indicated that at low temperatures, transport across the arrays occurs via a sequence of cotunneling events, each involving  $\approx 3$ –4 ITO NCs. At higher temperatures, the number of hops decreases to one and cotunneling behavior makes way for sequential tunneling. The results presented in this work also demonstrate the potential and functionality of these superlattices as novel transparent vapor sensing materials. Swelling of the NCs network as well as the permittivity changes seem to play major roles in the sensing mechanism. In conclusion, the fast response, high sensitivity, robustness under ambient condition, room-temperature operability, and optical transparency render phthalocyanine-coupled ITO NC superlattices promising materials for novel sensing applications.

## 5. Experimental Section

*Synthesis of ITO Nanocrystals:* MA-capped ITO nanocrystals were synthesized according to the method reported in our previous work.<sup>[43]</sup>

*Synthesis of Ligands:* Cu- and Zn-4,4',4'',4'''-tetraaminophthalocyanine (Cu- and Zn4APc) were synthesized following previously reported procedures.<sup>[77]</sup> Co-, Fe-, and Ni4APc were purchased from Abcr and used without further purification.

*Thin-Film Preparation and Ligand Exchange:* Electronically coupled NC superlattice thin-films were prepared by a Langmuir-type assembly at the liquid/air interface.<sup>[43,78–80]</sup> The fabrication process and ligand exchange were carried out in a home-built Teflon chamber according to our previously reported method.<sup>[43]</sup>

*Instrumentation:* The quality and the structure of NC thin-films, the thickness, and also the particle size and shape were verified by STEM on a Hitachi SU 8030 microscope operating at 30 kV. The presence of M4APc in the NC-thin films after ligand exchange was confirmed by XPS and UV-vis-NIR spectroscopy. XPS measurements were carried out using a photoelectron spectrometer which was equipped with a conventional XR50 X-ray source (Al  $K_{\alpha}$  working at 12.5 kV and 20 mA, 1486.61 eV) and a PHOIBOS 100 multi-channel detector analyzer (SPECS). The binding energies were corrected for electrical charge effects by referencing to Au4f and adventitious C1s peak, which were assumed to have a binding energy of 84.0 and 284.8 eV, respectively. The relative tin content was determined by the ratio of the Sn3d peak area to the total area of the In and Sn3d peaks, scaled by the relative photoionization cross-section for each element. Optical measurements were performed on solid state films on glass substrates using an UV-vis-NIR spectrometer (Agilent Technologies, Cary 5000). GISAXS was performed at a laboratory-based Xeuss 2.0 instrument from Xenocs, France, with a wavelength of 1.5405 Å (Cu  $K_{\alpha}$  source). A 2D Pilatus 300 K detector was employed at a distance of 2.5 m from the sample to collect the data. An incident beam of size  $0.5 \times 0.5$  ( $V \times H$ ) mm<sup>2</sup> was used at a grazing angle of 0.2° onto the sample surfaces. Electrical measurements on the NC arrays at room temperature were performed using a Keithley 2634B dual source-meter unit, controlled by the included test script builder program. The free-floating ligand-exchanged NC superlattices were deposited on a commercially available bottom-gate, bottom-contact transistor substrates (Fraunhofer Institute for Photonic Microsystems, Dresden, Germany) with interdigitated Au electrodes of 10 mm width and 2.5 μm channel length (distance between Au electrodes) followed by annealing at 250 °C for 2 h under nitrogen atmosphere. Substrates were contacted using a home-built probe station enclosed in a nitrogen glovebox. The temperature-dependent charge transport properties of the NC thin-films were measured by a Lake-Shore CRX-6.5K probe station and a Keithley 2636B dual source-meter unit. The temperature was controlled by a Lake Shore (Model 336) temperature controller.

For investigating the vapor sensing properties, NC superlattices were deposited on commercially available glass substrates with interdigitated gold electrode structure (90 finger pairs, 10  $\mu\text{m}$  microelectrode gap, and 10  $\mu\text{m}$  and 150 nm microelectrode width and height, respectively; ED-IDE1-Au micrux Technologies). The sensitivity of the films was characterized by dosing them with vapors of 4M2P, toluene, isopropanol, and water while monitoring their resistances at 0.1 V. All vapor sensing experiments were carried out at room temperature (ca. 25  $^{\circ}\text{C}$ ) with dried purified air as carrier gas using the previously reported commercial instrumentation.<sup>[81]</sup> Due to the integrated mass flow controllers in the system  $\approx 3\times$  to  $\approx 1000\times$  dilution of saturated test vapors is possible. With the vapor pressures of the analytes (21, 29, 20, and 23 mbar at 20  $^{\circ}\text{C}$ , respectively)<sup>[76]</sup> concentrations between 50 and 5000 ppm are possible. As all the mentioned test vapors have comparable vapor pressures, their interaction with the samples is expected to mainly arise from their chemical nature (polarity and structural features) and not from the differences in vapor pressure.

## Supporting Information

Supporting Information is available from the Wiley Online Library or from the author.

## Acknowledgements

The authors acknowledge the Deutsche Forschungsgemeinschaft (DFG) for support under Grants SCHE1905/3, SCHE1905/4, and SCHR700/25. The authors also thank Elke Nadler, Institute of Physical and Theoretical Chemistry, University of Tübingen, scanning electron microscopy (SEM) and STEM measurements using a Hitachi SU 8030 SEM which was funded by the DFG under contract INST 37/829-1 FUGG partially. The paper was written through contributions of all authors. All authors have given approval to the final version of the paper.

## Conflict of Interest

The authors declare no conflict of interest.

## Keywords

colloidal nanocrystals, indium tin oxide (ITO), multiple inelastic cotunneling, self-assembly, vapor sensors

Received: December 12, 2017

Revised: January 26, 2018

Published online:

- [1] M. Nasilowski, B. Mahler, E. Lhuillier, S. Ithurria, B. Dubertret, *Chem. Rev.* **2016**, *116*, 10934.
- [2] M. A. Boles, D. Ling, T. Hyeon, D. V. Talapin, *Nat. Mater.* **2016**, *15*, 141.
- [3] M. A. Boles, M. Engel, D. V. Talapin, *Chem. Rev.* **2016**, *116*, 11220.
- [4] J. Q. Grim, L. Manna, I. Moreels, *Chem. Soc. Rev.* **2015**, *44*, 5897.
- [5] G. H. Carey, A. L. Abdelhady, Z. J. Ning, S. M. Thon, O. M. Bakr, E. H. Sargent, *Chem. Rev.* **2015**, *115*, 12732.
- [6] D. V. Talapin, J. S. Lee, M. V. Kovalenko, E. V. Shevchenko, *Chem. Rev.* **2010**, *110*, 389.
- [7] W. J. Parak, D. Gerion, T. Pellegrino, D. Zanchet, C. Micheel, S. C. Williams, R. Boudreau, M. A. Le Gros, C. A. Larabell, A. P. Alivisatos, *Nanotechnology* **2003**, *14*, R15.

- [8] N. Vogel, M. Retsch, C. A. Fustin, A. del Campo, U. Jonas, *Chem. Rev.* **2015**, *115*, 6265.
- [9] K. D. Gilroy, A. Ruditskiy, H. C. Peng, D. Qin, Y. N. Xia, *Chem. Rev.* **2016**, *116*, 10414.
- [10] M. Scheele, W. Brütting, F. Schreiber, *Phys. Chem. Chem. Phys.* **2015**, *17*, 97.
- [11] R. A. Potyrailo, *Chem. Soc. Rev.* **2017**, *46*, 5311.
- [12] R. A. Potyrailo, *Chem. Rev.* **2016**, *116*, 11877.
- [13] K. Saha, S. S. Agasti, C. Kim, X. N. Li, V. M. Rotello, *Chem. Rev.* **2012**, *112*, 2739.
- [14] J. Zhang, Z. Y. Qin, D. W. Zeng, C. S. Xie, *Phys. Chem. Chem. Phys.* **2017**, *19*, 6313.
- [15] B. Skinner, T. R. Chen, B. I. Shklovskii, *Phys. Rev. B* **2012**, *85*, 205316.
- [16] B. I. Shklovskii, A. L. Efros, *Electronic Properties of Doped Semiconductors*, Springer, Berlin **1984**.
- [17] M. S. Kang, A. Sahu, D. J. Norris, C. D. Frisbie, *Nano Lett.* **2011**, *11*, 3887.
- [18] K. C. Beverly, J. F. Sampaio, J. R. Heath, *J. Phys. Chem. B* **2002**, *106*, 2131.
- [19] H. Liu, A. Pourret, P. Guyot-Sionnest, *ACS Nano* **2010**, *4*, 5211.
- [20] S. Bazargan, N. F. Heinig, J. F. Rios, K. T. Leung, *J. Phys. Chem. C* **2012**, *116*, 4979.
- [21] D. Yu, C. J. Wang, B. L. Wehrenberg, P. Guyot-Sionnest, *Phys. Rev. Lett.* **2004**, *92*, 216802.
- [22] I. S. Beloborodov, A. V. Lopatin, V. M. Vinokur, *Phys. Rev. B* **2005**, *72*, 125121.
- [23] T. B. Tran, I. S. Beloborodov, X. M. Lin, T. P. Bigioni, V. M. Vinokur, H. M. Jaeger, *Phys. Rev. Lett.* **2005**, *95*, 076806.
- [24] T. B. Tran, I. S. Beloborodov, J. S. Hu, X. M. Lin, T. F. Rosenbaum, H. M. Jaeger, *Phys. Rev. B* **2008**, *78*, 075437.
- [25] M. V. Feigel'man, A. S. Ioselevich, *JETP Lett.* **2005**, *81*, 277.
- [26] S. Blok, R. R. A. Mojarro, L. A. Maduro, M. Blaauboer, S. J. Van Der Molen, *J. Chem. Phys.* **2017**, *146*, 092325.
- [27] I. S. Beloborodov, A. Glatz, V. M. Vinokur, *Phys. Rev. B* **2007**, *75*, 052302.
- [28] D. V. Averin, Y. V. Nazarov, *Phys. Rev. Lett.* **1990**, *65*, 2446.
- [29] J. Dugay, R. P. Tan, M. Ibrahim, C. Garcia, J. Carrey, L. M. Lacroix, P. F. Fazzini, G. Viau, M. Respaud, *Phys. Rev. B* **2014**, *89*, 041406.
- [30] H. Moreira, Q. Yu, B. Nadal, B. Bresson, M. Rosticher, N. Lequeux, A. Zimmers, H. Aubin, *Phys. Rev. Lett.* **2011**, *107*, 176803.
- [31] R. W. Johns, M. A. Blemker, M. S. Azzaro, S. Heo, E. L. Runnerstrom, D. J. Milliron, S. T. Roberts, *J. Mater. Chem. C* **2017**, *5*, 5757.
- [32] B. M. Crockett, A. W. Jansons, K. M. Koskela, D. W. Johnson, J. E. Hutchison, *ACS Nano* **2017**, *11*, 7719.
- [33] E. L. Runnerstrom, A. Bergerud, A. Agrawal, R. W. Johns, C. J. Dahlman, A. Singh, S. M. Selbach, D. J. Milliron, *Nano Lett.* **2016**, *16*, 3390.
- [34] T. M. Mattox, X. Ye, K. Manthiram, P. J. Schuck, A. P. Alivisatos, J. J. Urban, *Adv. Mater.* **2015**, *27*, 5830.
- [35] S. D. Lounis, E. L. Runnerstrom, A. Llordés, D. J. Milliron, *J. Phys. Chem. Lett.* **2014**, *5*, 1564.
- [36] A. Agrawal, R. W. Johns, D. J. Milliron, *Annu. Rev. Mater. Res.* **2017**, *47*, 1.
- [37] T. R. Gordon, T. Paik, D. R. Klein, G. V. Naik, H. Caglayan, A. Boltasseva, C. B. Murray, *Nano Lett.* **2013**, *13*, 2857.
- [38] A. Andre, C. Theurer, J. Lauth, S. Maiti, M. Hodas, M. Samadi Khoshkhou, S. Kinge, A. J. Meixner, F. Schreiber, L. D. A. Siebbeles, K. Braun, M. Scheele, *Chem. Commun.* **2017**, *53*, 1700.
- [39] J. Zaumseil, K. W. Baldwin, J. A. Rogers, *J. Appl. Phys.* **2003**, *93*, 6117.
- [40] J. F. Dayen, E. Devid, M. V. Kamalakar, D. Golubev, C. Guedon, V. Faramarzi, B. Doudin, S. J. van der Molen, *Adv. Mater.* **2013**, *25*, 400.
- [41] A. G. Zabrodskii, *Philos. Mag. B* **2001**, *81*, 1131.
- [42] M. Harbeck, D. D. Erbahar, I. Gurol, E. Musluoglu, V. Ahsen, Z. Z. Ozturk, *Sens. Actuators, B* **2011**, *155*, 298.

- [43] M. Samadi Khoshkhoo, S. Maiti, F. Schreiber, T. Chassé, M. Scheele, *ACS Appl. Mater. Interfaces* **2017**, *9*, 14197.
- [44] G. L. Stansfield, P. J. Thomas, *J. Am. Chem. Soc.* **2012**, *134*, 11888.
- [45] C. Duan, Y. Wang, J. L. Sun, C. R. Guan, S. Grunder, M. Mayor, L. M. Peng, J. H. Liao, *Nanoscale* **2013**, *5*, 10258.
- [46] A. J. Quinn, P. Beecher, D. Iacopino, L. Floyd, G. De Marzi, E. V. Shevchenko, H. Weller, G. Redmond, *Small* **2005**, *1*, 613.
- [47] P. Beecher, A. J. Quinn, E. V. Shevchenko, H. Weller, G. Redmond, *Nano Lett.* **2004**, *4*, 1289.
- [48] C. T. Black, C. B. Murray, R. L. Sandstrom, S. H. Sun, *Science* **2000**, *290*, 1131.
- [49] B. Laikhtman, E. L. Wolf, *Phys. Lett. A* **1989**, *139*, 257.
- [50] B. Abeles, P. Sheng, M. D. Coutts, Y. Arie, *Adv. Phys.* **1975**, *24*, 407.
- [51] A. M. Saleh, S. M. Hraibat, R. M. L. Kitaneh, M. M. Abu-Samreh, S. M. Musameh, *J. Semicond.* **2012**, *33*, 082002.
- [52] S. Samanta, D. K. Aswal, A. Singh, A. K. Debnath, M. S. Kumar, Y. Hayakawa, S. K. Gupta, J. V. Yakhmi, *Appl. Phys. Lett.* **2010**, *96*, 013305.
- [53] T. D. Anthopoulos, T. S. Shafai, *Phys. Status Solidi A* **2000**, *181*, 569.
- [54] R. D. Gould, R. I. R. Blyth, *Phys. Status Solidi A* **1990**, *120*, K57.
- [55] R. D. Gould, *J. Phys. D: Appl. Phys.* **1986**, *19*, 1785.
- [56] J. S. Zhang, B. I. Shklovskii, *Phys. Rev. B* **2004**, *70*, 115317.
- [57] R. Rosenbaum, *Phys. Rev. B* **1991**, *44*, 3599.
- [58] I. S. Beloborodov, A. V. Lopatin, V. M. Vinokur, K. B. Efetov, *Rev. Mod. Phys.* **2007**, *79*, 469.
- [59] I. S. Beloborodov, A. V. Lopatin, V. M. Vinokur, *Phys. Rev. B* **2005**, *72*, 125121.
- [60] E. E. Havinga, *J. Phys. Chem. Solids* **1961**, *18*, 253.
- [61] V. Bobnar, A. Levstik, C. Huang, Q. M. Zhang, *Phys. Rev. B* **2005**, *71*, 041202.
- [62] A. Yazici, N. Unus, A. Altindal, B. Salih, O. Bekaroglu, *Dalton Trans.* **2012**, *41*, 3773.
- [63] M. Pauly, J. F. Dayen, D. Golubev, J. B. Beaufrand, B. P. Pichon, B. Doudin, S. Begin-Colin, *Small* **2012**, *8*, 108.
- [64] K. Yakushiji, S. Mitani, F. Ernult, K. Takanashi, H. Fujimori, *Phys. Rep.* **2007**, *451*, 1.
- [65] S. Mitani, S. Takahashi, K. Takanashi, K. Yakushiji, S. Maekawa, H. Fujimori, *Phys. Rev. Lett.* **1998**, *81*, 2799.
- [66] H. Sukegawa, S. Nakamura, A. Hirohata, N. Tezuka, K. Inomata, *Phys. Rev. Lett.* **2005**, *94*, 866.
- [67] A. Hirohata, K. Takanashi, *J. Phys. D: Appl. Phys.* **2014**, *47*, 193001.
- [68] G. L. E. Turner, *Ann. Sci.* **1991**, *48*, 496.
- [69] P. N. Bartlett, S. K. Ling-Chung, *Sens. Actuators* **1989**, *19*, 141.
- [70] Y. Joseph, B. Guse, A. Yasuda, T. Vossmeier, *Sens. Actuators, B* **2004**, *98*, 188.
- [71] A. Kumar, J. Brunet, C. Varenne, A. Ndiaye, A. Pauly, M. Penza, M. Alvisi, *Sens. Actuators, B* **2015**, *210*, 398.
- [72] A. Belghachi, R. A. Collins, *J. Phys. D: Appl. Phys.* **1990**, *23*, 223.
- [73] A. Belghachi, R. A. Collins, *J. Phys. D: Appl. Phys.* **1988**, *21*, 1647.
- [74] E. I. Martin, J. M. Martinez, E. S. Marcos, *J. Chem. Phys.* **2011**, *134*, 024503.
- [75] Y. Joseph, B. Guse, T. Vossmeier, A. Yasuda, *J. Phys. Chem. C* **2008**, *112*, 12507.
- [76] Y. Joseph, A. Peic, X. D. Chen, J. Michl, T. Vossmeier, A. Yasuda, *J. Phys. Chem. C* **2007**, *111*, 12855.
- [77] S. H. Jung, J. H. Choi, S. M. Yang, W. J. Cho, C. S. Ha, *Mater. Sci. Eng. B* **2001**, *85*, 160.
- [78] R. Sharma, A. M. Sawvel, B. Barton, A. G. Dong, R. Buonsanti, A. Lordes, E. Schaible, S. Axnanda, Z. Liu, J. J. Urban, D. Nordlund, C. Kisielowski, D. J. Milliron, *Chem. Mater.* **2015**, *27*, 2755.
- [79] A. Dong, Y. Jiao, D. J. Milliron, *ACS Nano* **2013**, *7*, 10978.
- [80] A. G. Dong, J. Chen, S. J. Oh, W. K. Koh, F. X. Xiu, X. C. Ye, D. K. Ko, K. L. Wang, C. R. Kagan, C. B. Murray, *Nano Lett.* **2011**, *11*, 841.
- [81] Y. Joseph, I. Besnard, M. Rosenberger, B. Guse, H. G. Nothofer, J. M. Wessels, U. Wild, A. Knop-Gericke, D. S. Su, R. Schlögl, A. Yasuda, T. Vossmeier, *J. Phys. Chem. B* **2003**, *107*, 7406.